

# Zircon growth experiments reveal limited equilibrium Zr isotope fractionation in magmas

H.G.D. Tompkins, M. Ibañez-Mejía, F.L.H. Tissot, E. Bloch, Y. Wang, and D. Trail

## Supplementary Information

The Supplementary Information includes:

- Methods
- Zircon Isotope Data Processing and Modelling Approach
- Supplementary Tables S-1 to S-5
- Figures S-1 to S-6
- Supplementary Information References

## Methods

### Processing of Experimental Products

Molybdenum (Mo) – Platinum (Pt) experimental capsules from the study of Wang and Trail (2019) were marked and sliced in half using a sagittal cut with a wire-saw. Only one half of each experimental product was used for this study and the other half was preserved. Capsules were first bathed in 100 ml of concentrated aqua regia for ~72 hours in glass beakers to fully dissolve the Mo outer sleeves surrounding the Pt capsules. Once the Mo sleeve had fully dissolved, the remaining Pt capsules were rinsed multiple times with distilled H<sub>2</sub>O and sonicated in 2 % HNO<sub>3</sub> for 30 minutes to ensure all aqua regia and Mo contamination was removed. Without the Mo outer sleeves, the experimental products were easily freed from the thin inner Pt capsules by bending them with a finger. The resulting glass and zircon mixtures were mechanically broken and two small fragments from each run were picked and mounted in epoxy for Secondary Ion Mass Spectrometry (SIMS). The remaining material for each experiment was ground manually under ethanol for 5 minutes using an ultra-high purity corundum mortar and pestle, which had been pre-cleaned twice before processing each experiment by grinding ultra-high-purity silica sand (>99.995% purity) obtained from AdValue Technology. Once reduced to a fine powder, samples were transferred into a pre-cleaned glass beaker by pipetting the ethanol-powder slurry before bringing them into the clean laboratory. The remaining steps were performed inside a Class 1000 clean laboratory supplied with HEPA-filtered air, and inside ULPA-filtered vertical laminar flow hoods that provide a local environment better than Class 100 and closer to Class 10. Samples were transferred into pre-cleaned 7 ml Teflon beakers in 500 µl ethanol and an additional 5 ml of MQ-H<sub>2</sub>O were added to dilute the alcohol. Teflon beakers were left uncapped on a hot plate at 70 °C overnight to drive off the alcohol and H<sub>2</sub>O was evaporated until only ~100 µl of liquid remained.

### Chemical Separation

Because the small ( $\leq 20$  µm) zircon produced by our experiments cannot be physically separated from the glass, a chemical separation procedure using a series of stepwise leaches was developed. Leaching steps, designed and calibrated to efficiently remove the glass while leaving zircon unreacted, were performed using

3.5 M HNO<sub>3</sub> and variable HF concentration. Figure S-1 shows the results of our final calibration run, where an experimental zircon-glass mixture was subjected to multiple low pressure (*i.e.*, capped beaker in a hot plate at room pressure) acid attack steps with variable HF concentration increasing from 0.1 to 28 M. Because the starting mix was doped with rubidium (Rb), a highly incompatible element in the zircon structure (Thomas *et al.*, 2002), the Rb concentration of each step was used to monitor glass removal and the quality of the chemical separation. As shown in Figure S-1, all Rb was extracted during the first two leaching steps using 0.1 and 0.2 M HF at low pressure, indicating complete glass dissolution at low HF molarities while leaving zircon completely unreacted. No Zr release above instrumental background was observed in any subsequent low-pressure steps ranging from 0.5 to 28 M HF, and Zr from zircon was only extracted after performing a high-pressure dissolution step using a Parr digestion vessel and 28 M HF for 72 hours at 215 °C.

Once calibrated, our final protocol consisted of only five low-pressure leaching steps (*i.e.*, 3.5 M HNO<sub>3</sub> + 0.1 M HF, 3.5 M HNO<sub>3</sub> + 0.2 M HF, 3.5 M HNO<sub>3</sub> + 0.75 M HF, 3.5 M HNO<sub>3</sub> + 1.5 M HF, and 15 M HF). The first three leaching steps (glass cut) were combined in a 30 ml Teflon beaker. The 1.5 M and 15 M HF steps were collected separately for concentration measurements of Rb and Zr to verify that glass had been completely removed during the first three leaching steps and that zircon was not being attacked. All concentrations were measured using a quadrupole – inductively coupled plasma - mass spectrometer (Q-ICP-MS) in the Trail lab at University of Rochester. Rb and Zr counts were below the detection limit in all (1.5+15) M HF leaching solutions, confirming that our protocol achieved complete dissolution of glass and complete glass-zircon separation over the first three leaching steps. After confirmation that all glass had been removed, 3 ml of 28 M HF + 1 drop 16 M HNO<sub>3</sub> was added to the beakers, and these were loaded inside a 125 ml high-pressure Parr® vessel. Complete digestion was achieved after ~72 hours at 215 °C.

In addition to the zircon-glass experimental products, four bulk starting materials (base mixes) from which the experiments were synthesized were also dissolved for Zr isotope measurements. Approximately 10 mg of these homogenized synthetic powders were loaded into 7 ml Teflon beakers with 3 ml of 28 M HF + 1 drop 16 M HNO<sub>3</sub>. Beakers were then loaded inside a high-pressure Parr® vessel for 48 hours at 215 °C. Ca-fluoride salts that formed after digestion of base mixes using concentrated HF were completely removed using repeated dry-down and re-digestion steps with 3 M HNO<sub>3</sub> + 0.4 M H<sub>3</sub>BO<sub>3</sub>, by preferential production and evaporation of volatile BF<sub>3</sub>.

### Spiking and Chromatographic Purification of Zr

Once all zircon, glass, and bulk base mixes were fully in solution, the Zr concentration of all fractions were measured by Q-ICP-MS using gravimetrically prepared calibration standards to ensure accurate spiking. Following concentration measurements, aliquots containing ~495 ng of sample Zr were transferred into clean 7 ml Teflon beakers and mixed with ~405 ng of Zr from a calibrated <sup>91</sup>Zr-<sup>96</sup>Zr DS to achieve an optimal spiking ratio (*i.e.*, 0.45 spike: 0.55 sample; Tompkins *et al.*, 2020). To achieve sample-spike equilibration, samples were fluxed in a capped beaker at 130 °C on a hot plate overnight, dried down completely, redigested in 1 ml of 16 M HNO<sub>3</sub>, fluxed overnight, and dried down a second time. Samples were then re-digested using 5 ml of a 3 M HNO<sub>3</sub>-0.4 M H<sub>3</sub>BO<sub>3</sub> mixture for chromatographic purification.

Zirconium was chemically purified by ion-exchange chromatography using the methods described in Tompkins *et al.* (2020). In brief, Zr and Hf were first separated from major elements using 2 ml Eichrom TODGA resin (Pourmand and Dauphas, 2010; Ibañez-Mejia and Tissot, 2019). A “matrix clean-up” step was then performed using Bio-Rad AG1-X8 columns (150 µl volume) to ensure complete removal of Fe and other major elements. Subsequently, Zr was separated from Hf using Eichrom Ln-spec resin, and from Mo and Ru, which are isobaric interferences on several Zr isotopes, using a final clean-up step with AG1-X8 resin. This procedure resulted in total procedural Zr yields >90% and total Mo/Zr < 4x10<sup>-4</sup>. Three total procedural blanks (spiked with ca. 60 ng of Zr DS) were processed and measured during this study. All blanks yielded <1 ng



total Zr, which is three orders of magnitude smaller than the amount of sample Zr utilized for each measurement and thus considered negligible. More details on the chemical purification procedures are provided in Tompkins *et al.* (2020) and Klaver *et al.* (2021).

Purified Zr solutions were dried completely and then fluxed in 1 ml 16 M HNO<sub>3</sub> + 1 ml 15 wt. % H<sub>2</sub>O<sub>2</sub> for several hours to drive off any remaining organics from the resins. Samples were fully dried again, then taken up in 1 ml 16 M HNO<sub>3</sub> + 0.5 ml 28 M HF in capped beakers to re-digest, and gently dried down to a small bead before taking up ~3 ml of 0.59 M HNO<sub>3</sub> + 0.28 M HF. After fluxing overnight in capped beakers at 100 °C, 100 µl aliquot were taken for Zr concentration measurement on the multicollector inductively coupled plasma mass spectrometer (MC-ICP-MS) and to verify complete Mo removal. Samples were then diluted to a final Zr concentration of 60 ng/g in 0.59 M HNO<sub>3</sub> + 0.28 M HF for MC-ICP-MS measurements.

### Mass Spectrometry

Zr isotopic measurements were performed with a Thermo Scientific Neptune Plus using an Aridus 3 desolvating nebulizer at the Isotoparium, California Institute of Technology, following the methods of Tompkins *et al.* (2020). Measurements were performed in low mass resolution, using a static configuration monitoring masses 90 through 98. All Faraday cups were assigned 10<sup>11</sup> Ω feedback resistors except for H1 (<sup>95</sup>Mo) and H4 (<sup>98</sup>Mo), which were assigned 10<sup>12</sup> Ω feedback resistors to improve accuracy of Mo isobaric interference monitoring and corrections. Cup gains were calibrated daily.

Each unknown measurement was bracketed by measurements of the NIST RM8299 Zr iRM, a new Zr isotopic reference material prepared in a collaboration between the Isotoparium, the Arizona Heavy Isotopes Laboratory, and the U.S. National Institute of Standards and Technology (NIST) (Tissot *et al.*, 2022). Bracketing standards were spiked at the same level as the samples. On-peak-zeros (OPZ) were measured before all samples and standards using a 50 s uptake and 20 s on-peak measurement of clean acid solution from the same batch used to dilute the samples, to monitor memory effects of the sample introduction system and remove background from all measurements. Sample and bracketing standard measurements consisted of 50 s of sample uptake, followed by 50 cycles of 4.192 s integration time each, for a total 210 s of static on-peak sample measurement. The Aridus 3 was rinsed for 360 s between samples using 0.59 M HNO<sub>3</sub> + 0.56 M HF, before repeating the cycle for the next standard/unknown.

Within each sequence, two types of secondary reference materials were measured to monitor mass spectrometer performance and ensure data accuracy: 1) an industrial, pure Zr solution obtained from SPEX and calibrated by Tompkins *et al.* (2020); and 2) bulk-rock geostandard materials subjected to the same chemical processing as the samples studied here. The purpose of this approach is two-fold: 1) the SPEX solution allows monitoring the performance of the sample introduction system and mass spectrometer only, without any potentially complicating factors introduced by the ion exchange chemistry; and 2) results from geostandards allow monitoring the entire process, from sample dissolution, through chemistry and mass spectrometry, therefore demonstrating accuracy for our complete procedure.

The results of all reference materials measured during this study are shown in Figure S-2, where they are compared to their respective reference values. The excellent agreement between the measured  $\delta^{94/90}\text{Zr}_{\text{NIST}}$  of these reference materials relative to published values demonstrates the accuracy of our results and ensures compatibility of our zircon-melt fractionation calculations relative to the existing Zr isotope literature.

### Zirconium concentration measurements of glass by secondary ion mass spectrometry (SIMS)

Small fragments of each experiment were mounted in epoxy for trace element measurements of glass using secondary ion mass spectrometry (SIMS). SIMS analyses were performed using the CAMECA 1280HR SIMS instrument housed in the Swiss SIMS laboratory within the Center for Advanced Surface Analysis (CASA) at the University of Lausanne. Mounts were coated with ~35 nm of Au, deposited by Au evaporation or sputter coating under vacuum, prior to analysis. Analyses included positive secondary ions of  $^{28}\text{Si}$ ,  $^{30}\text{Si}$ ,  $^{85}\text{Rb}$ ,  $^{90}\text{Zr}$  and  $^{180}\text{Hf}$ . Samples were sputtered with an  $^{16}\text{O}^{2-}$  primary ion beam (PIB) generated using a Hyperion-II RF plasma source, which was accelerated at 13 kV and focused to a ~4  $\mu\text{m}$  spot. Secondary ions were accelerated at 10 kV. Analyses consisted of 90 s of pre-sputtering followed by 15 cycles with integration times of 2, 2, 8, 8 and 6 s, respective to the list of measured secondary ions above. Between pre-sputtering and measurement, the secondary ion beam was automatically centered within the transfer and field apertures; likewise, the secondary high voltage was automatically adjusted to compensate for sample charging if necessary. Analyses were standardized using NIST 610 and zircon 91500, both of which were measured once between every 4 unknown spots. Data processing was performed using a customized MATLAB reduction code using standard-sample-bracketing relative to the known Si and Zr concentrations of NIST 610 and zircon 91500, and the Rb concentration of NIST 610.

### Constraining fractional Zr removal from the liquid ( $f$ )

The value of  $f$ , *i.e.*, the fraction of Zr removed from the liquid during each experimental run, was constrained using two independent approaches: i) using the *in-situ* determinations of Zr concentration in the glass from SIMS measurements; and ii) using Zr/Rb measurements from solutions produced after acid leaching during preparation for isotopic analyses. These two approaches and the mass-balance equations used are as follows:

#### Approach 1 – using *in-situ* glass [Zr] determinations

Given that the starting Zr concentration of each experiment (hereafter  $[\text{Zr}]_{\text{bulk}}$ ) is known from the masses of the high-purity oxides used to make the starting base mixes (from Wang and Trail, 2019), we can use the concentration of Zr in the glass (hereafter  $[\text{Zr}]_{\text{glass}}$ ) to determine the fraction of Zr removed from the liquid,  $f$ , using the following relation:

$$f = 1 - \frac{[\text{Zr}]_{\text{glass}}}{[\text{Zr}]_{\text{bulk}}} \quad \text{Eq. S-1}$$

$[\text{Zr}]_{\text{glass}}$  values were determined *in-situ* using multiple SIMS spot analyses place in two randomly selected glass fragments set aside from each experimental run, prior to grinding and dissolution. The advantage of this approach is that, in addition to allowing quantification of a mean  $f$  for each experimental run product, it also allows evaluation of the spatial heterogeneity of  $[\text{Zr}]_{\text{glass}}$ . We use this spatial variability in  $[\text{Zr}]_{\text{glass}}$  to assign an uncertainty to  $f$  that was then propagated through all subsequent calculations described below. Mean values of  $[\text{Zr}]_{\text{glass}}$ , calculated  $f$  values, and uncertainties assigned to both of these parameters, are reported in Table S3. These were calculated as the mean and standard deviation of all SIMS  $[\text{Zr}]_{\text{glass}}$  determinations made in glass from each experiment.

#### Approach 2 – verifying $f$ using bulk Zr/Rb measurements in solutions after acid leaching of glass

In order to verify the mean  $f$  values determined from Approach 1 above, a mass balance approach using the bulk Zr/Rb elemental ratios measured on aliquots of the experiments after dissolution was also performed. All fractions of glass, zircon, as well as the starting bulk base mixes analyzed for  $\delta^{94/90}\text{Zr}$ , were measured via Q-

ICPMS for Zr concentrations and Zr/Rb ratios to verify effective zircon-glass separation and to ensure accurate spiking. In the equations below,  $X_{\text{glass}}$  is taken to represent the mass fraction of liquid remaining in each experiment at quenching,  $X_{\text{zircon}}$  is the mass fraction of zircon formed in each experiment, and  $f_{\text{Zr/Rb}}$  is the effective magnitude of  $f$  for the bulk glass constrained using this second approach. This second method using bulk solution measurements for constraining  $f$  provides a good consistency check of the *in-situ* method (Approach 1), but has the drawback that it erases (homogenizes) any spatial variability of  $[\text{Zr}]_{\text{glass}}$  present within the glass, and therefore does not allow propagation of  $f$  variability through the isotope fractionation calculations described below. As such, we report values of  $f_{\text{Zr/Rb}}$  in Table S3 as a consistency check, but the values of  $f$  and its standard deviation constrained using Approach 1 are preferred for all subsequent calculations and uncertainty propagations.

We can write mass balance equations for Rb and Zr in each experiment as:

$$[\text{Rb}]_{\text{bulk}} = [\text{Rb}]_{\text{glass}} \cdot X_{\text{glass}} + [\text{Rb}]_{\text{zircon}} \cdot (1 - X_{\text{glass}}) \text{ Eq. S-2}$$

and,

$$[\text{Zr}]_{\text{bulk}} = [\text{Zr}]_{\text{glass}} \cdot X_{\text{glass}} + [\text{Zr}]_{\text{zircon}} \cdot (1 - X_{\text{glass}}) \text{ Eq. S-3}$$

Dividing Eq. S-2 by Eq. S-3 yields

$$\left(\frac{\text{Rb}}{\text{Zr}}\right)_{\text{bulk}} = \frac{[\text{Rb}]_{\text{glass}} \cdot X_{\text{glass}} + [\text{Rb}]_{\text{zircon}} \cdot (1 - X_{\text{glass}})}{[\text{Zr}]_{\text{glass}} \cdot X_{\text{glass}} + [\text{Zr}]_{\text{zircon}} \cdot (1 - X_{\text{glass}})} \text{ Eq. S-4}$$

which upon re-arranging can be written as

$$\left(\frac{\text{Zr}}{\text{Rb}}\right)_{\text{bulk}} = \frac{[\text{Zr}]_{\text{glass}}}{[\text{Rb}]_{\text{glass}}} + \frac{[\text{Zr}]_{\text{zircon}}}{[\text{Rb}]_{\text{glass}}} \left(\frac{1}{X_{\text{glass}}} - 1\right) \text{ Eq. S-5}$$

Given the strong incompatibility of Rb in the zircon structure (Thomas *et al.*, 2002), it is safe to assume that  $[\text{Rb}]_{\text{zircon}}=0$ , and one can re-write Eq. S-2 as

$$\frac{[\text{Rb}]_{\text{bulk}}}{X_{\text{glass}}} = [\text{Rb}]_{\text{glass}} \text{ Eq. S-6}$$

By substituting Eq. S-6 into Eq. S-5 and re-arranging terms, one can solve for  $X_{\text{glass}}$  as

$$X_{\text{glass}} = 1 - \frac{\left(\frac{\text{Zr}}{\text{Rb}}\right)_{\text{bulk}} - \left(\frac{\text{Zr}}{\text{Rb}}\right)_{\text{glass}}}{\frac{[\text{Zr}]_{\text{zircon}}}{[\text{Rb}]_{\text{bulk}}}} \text{ Eq. S-7}$$

The fraction of zircon ( $X_{\text{zircon}}$ ) formed in each experiment can be calculated as:

$$X_{\text{zircon}} = 1 - X_{\text{glass}} \text{ Eq. S-8}$$

And given that the fraction of Zr removed from the liquid in the form of zircon can be expressed as:

$$f_{\text{ZrRb}} = \frac{[\text{Zr}]_{\text{zircon}} \cdot X_{\text{zircon}}}{[\text{Zr}]_{\text{bulk initial}}} \text{ Eq. S-9}$$

Equations S-7, S-8, and S-9 can be combined into a final expression for determining a mean  $f_{\text{RbZr}}$  for each experiment, as follows:





$$f_{ZrRb} = \frac{[Zr]_{zircon} \cdot \left( 1 - \left( 1 - \frac{(\frac{Zr}{Rb})_{bulk} - (\frac{Zr}{Rb})_{glass}}{[\frac{Zr}{Rb}]_{zircon}} \right) \right)}{[Zr]_{bulk\ initial}} \quad \text{Eq. S-10}$$

For these calculations, zirconium in zircon was assumed to be stoichiometric (*i.e.*,  $[Zr]_{zircon} = 49.77$  wt. %), and  $[Zr]_{bulk}$  and  $[Rb]_{bulk}$  were calculated using the known concentrations of the starting oxides and their masses in the base mixtures as reported by Wang and Trail (2019). The values for  $(Zr/Rb)_{glass}$  used for  $f_{RbZr}$  calculations are those determined directly from our experiment dissolutions, measured by Q-ICPMS. The calculated values of  $f_{RbZr}$  determined this way are reported in Table S3, where they are compared with the values of  $f$  determined using our first calculation approach described above. The calculated values of  $f_{RbZr}$  are in excellent agreement with the mean  $f$  values estimated for  $[Zr]_{glass}$  via SIMS, thus lending further confidence of our calculations of Zr fractional removal.

As mentioned above, the mean and standard deviation of  $f$  determined using SIMS measurements in glass are the preferred values of  $f$  used for all  $\alpha$  calculations for two main reasons: i) the in-situ approach allows us to evaluate the spatial variability of Zr removal within each experiment, and thus assign an uncertainty to  $f$  for uncertainty propagations; and ii) the variability in the glass allows us to evaluate how far (or close) each experiment was from equilibrium at the time of quenching, which is a qualitative indicator of the magnitude of the Zr concentration gradients within the liquid at time of quenching. The distribution of  $[Zr]_{glass}$  values, calculated from  $n = 20\text{--}90$  spot determinations of Zr concentration in experimental glasses via SIMS, are shown in Figure S-5. Distributions of Zr concentrations are shown as kernel density estimates (KDE) using a Gaussian smoothing kernel and optimal bandwidths for each distribution calculated using the methods of Botev *et al.* (2010). Graphs were plotted using the *DensityDist* Matlab code of Pullen *et al.* (2014). It is clear from Figure S-5 that glasses from high-T (low- $f$ ) experiments exhibit a much larger spatial variability in  $[Zr]_{glass}$ , and that this variability in  $[Zr]_{glass}$  decreases with increasing mean  $f$ , reflecting the progressive obliteration of diffusive boundary layers in the liquid as Zr removal from the liquid increases.

## Zr Isotope Data Processing and Modelling Approach

### Verification of Zr mass-balance for experimental run products

An important first step to data interpretation is to verify that zirconium concentration and isotopic composition of measured glass and bulk zircon pairs conform to mass-balance with respect to known starting bulk compositions. For each experimental glass-zircon pair, the fraction of Zr removed from the liquid ( $f$ ) as well as the isotopic composition (expressed as  $\delta^{94/90}\text{Zr}$ ) for the two phases and their associated uncertainties was determined (Tables S2 and S3). Using mass-balance, the *reconstructed* bulk isotopic composition of a two-component mixture ( $R_{mix}$ ) between the measured glass ( $R_{glass}$ ) and zircon ( $R_{zircon}$ ) can be calculated as:

$$\left( \frac{{}^{94}\text{Zr}}{{}^{90}\text{Zr}} \right)_{mix} = \left( \frac{{}^{94}\text{Zr}}{{}^{90}\text{Zr}} \right)_{glass} \cdot \left( \frac{{}^{90}\text{Zr}_{glass}}{{}^{90}\text{Zr}_{mix}} \right) \cdot (1 - f) + \left( \frac{{}^{94}\text{Zr}}{{}^{90}\text{Zr}} \right)_{zircon} \cdot \left( \frac{{}^{90}\text{Zr}_{zircon}}{{}^{90}\text{Zr}_{mix}} \right) \cdot f \quad \text{Eq. S-11}$$

Expressing the  ${}^{94/90}\text{Zr}$  values in Eq. S-11 using delta notation, and because the concentrations of isotope  ${}^{90}\text{Zr}$  (*i.e.*, the most abundant isotope of Zr) are very close to equal in the zircon and in the glass (*i.e.*,  $[{}^{90}\text{Zr}]_{glass} \approx [{}^{90}\text{Zr}]_{zircon} \approx [{}^{90}\text{Zr}]_{mix}$ ), this expression can be reduced to

$$\delta^{94/90}\text{Zr}_{mix} = \delta^{94/90}\text{Zr}_{glass} \cdot (1 - f) + \delta^{94/90}\text{Zr}_{zircon} \cdot f \quad \text{Eq. S-12}$$



Using the calculated  $f$  values for each experiment (Table S2), and their respective  $\delta^{94/90}\text{Zr}$  for each glass-zircon pair (Table S3), a reconstructed  $\delta^{94/90}\text{Zr}$  value for the mix is calculated and compared with the starting  $\delta^{94/90}\text{Zr}$  of the experiments (*i.e.*,  $\delta^{94/90}\text{Zr}$  of base mixes) to assess mass balance. Calculation of Eq. S-12 was conducted using a Monte Carlo approach with  $10^5$  realizations and assuming normal distributions for all parameters, to obtain a value of the mix that considers all uncertainties. The result of these calculations is shown in Figure 1b of the main text, where it is compared to the mean  $\delta^{94/90}\text{Zr}$  of all base mixes (gray horizontal band). From these calculations it can be seen that all experiments except ZrGT13 conform to mass-balance with respect to the starting bulk  $\delta^{94/90}\text{Zr}$  composition within uncertainties, therefore reinforcing the notion that we can use the  $\delta^{94/90}\text{Zr}$  values determined from these three components (bulk, glass and zircon) to approximate  $\alpha_{\text{zircon-melt}}$  as follows below. Two reasons that can explain the small offset of ZrGT13 from perfect mass balance can be: i) the distribution of  $[\text{Zr}]_{\text{glass}}$  determined via SIMS spot analyses from glass fragments that were not digested may be an imperfect descriptor of the true variability of  $f$  (*i.e.*, internal compositional gradients) present in the liquid at the time of quenching to a glass; and/or ii) because the entire run product was not analyzed (*i.e.*, experimental capsules were first sliced in half longitudinally and only ~one half of the load mass, minus fragments set aside for SIMS, were analyzed for  $\delta^{94/90}\text{Zr}$ ), the strong compositional gradients present within the glass mean that small deviations from ideal mass-balance can be expected. Nevertheless, as pointed out above, only one experiment deviates from mass-balance expectations, and this experiment is therefore not given weight towards our final interpretations.

#### Quantifying the isotopic fractionation coefficient, $\alpha_{\text{zircon-melt}}$

Due to the slow diffusivity of tetravalent ions in zircon (Cherniak *et al.*, 1997), the growth of zircon from a magma (natural or experimental) removes Zr as a Rayleigh-type process even if chemical and isotopic equilibrium partitioning between the solid and melt are maintained (Ibañez-Mejía and Tissot, 2019). In an equilibrium Rayleigh-type system, the isotopic compositions of the evolving liquid, instantaneous solid, and bulk solid can be expressed using the following equations (Criss, 1999):

$$R_{\text{liq}} = R_0 f^{\alpha-1} \quad \text{Eq. S-13}$$

$$R_{\text{inst solid}} = R_0 \alpha f^{\alpha-1} \quad \text{Eq. S-14}$$

$$R_{\text{bulk solid}} = \frac{R_0 - R_{\text{liq}} f}{(1-f)} \quad \text{Eq. S-15}$$

where  $R_0$  is the initial isotopic composition of the bulk system,  $R_{\text{liq}}$  is the isotopic composition of the liquid,  $R_{\text{inst solid}}$  and  $R_{\text{bulk solid}}$  are the isotopic compositions of the instantaneous and bulk solids removed from the liquid, respectively,  $\alpha$  is the equilibrium fractionation coefficient between solid and liquid, and  $f$  is the fraction of Zr removed from the liquid in the form of solid. No fractionation occurs when  $\alpha_{\text{zircon-melt}} = 1$ . Larger fractionations result in a greater magnitude of divergence from 1. A graphical representation of the evolution of a Rayleigh-type system is shown in Figure S-3a, where the curves represented by Eqs. S-13 through S-15 are highlighted for greater clarity.

The Zr isotopic fractionation coefficient between zircon and melt  $\alpha_{\text{zircon-melt}}$ , is defined as follows:

$$\alpha_{\text{zircon-melt}} = \frac{R_{\text{inst solid}}}{R_{\text{liq}}} \quad \text{Eq. S-16}$$

Eq. S-16 implies that one could directly determine  $\alpha_{\text{zircon-melt}}$  if one could measure the isotopic composition of a liquid and instantaneous solid pair in direct equilibrium. However, as zircon crystals progressively grow from a liquid, they integrate multiple layers with variable  $R_{\text{inst solid}}$  (Eq. S-14) as their surrounding melt evolves following Eq. S-13 to produce a zoned, growth-integrated  $R_{\text{bulk solid}}$  (Eq. S-15). Given our experimental

approach as described in the Methods section above,  $R_{\text{inst solid}}$  is an unmeasurable value, and our experiments can only recover  $R_{\text{bulk solid}}$  for each run. Therefore, since we cannot calculate  $\alpha_{\text{zircon-melt}}$  directly, we calculate it by inversion of this Rayleigh-type system. Below we identify four distinct solutions to approximate  $\alpha_{\text{zircon-melt}}$  using our measurements:

#### Solution 1 – apparent $\alpha$ , or $\alpha_{\text{app}}$ :

The simplest yet arguably least accurate way of approximating  $\alpha$  from our experiments would be to calculate an apparent value (dubbed ‘ $\alpha_{\text{app}}$ ’) directly from the measured  $R_{\text{bulk solid}}$  and  $R_{\text{liq}}$  values, as follows:

$$\alpha_{\text{app}} = \frac{R_{\text{bulk solid}}}{R_{\text{liq}}} \quad \text{Eq. S-17}$$

In contrast to  $R_{\text{inst solid}}$ ,  $R_{\text{bulk solid}}$  is a measured quantity from our experiments. However, because  $R_{\text{bulk solid}}$  represents only the mean composition of a growth-zoned zircon,  $\alpha_{\text{app}}$  does not accurately reflect the magnitude of  $\alpha_{\text{zircon-melt}}$ , but rather provides a maximum permissible value of the latter. This is illustrated in Figure S-3b where, using a pre-imposed  $\alpha_{\text{zircon-melt}}=0.99997$  (see Fig. S-3a), the values of  $\alpha_{\text{zircon-melt}}$  and  $\alpha_{\text{app}}$  were calculated using Eqs. S-16 and S-17, respectively, as a function of  $f$ . It can be concluded from Figure S-3b that: i) the magnitude of  $\alpha_{\text{app}}$  always overestimates the magnitude of the ‘true’  $\alpha_{\text{zircon-melt}}$ ; ii)  $\alpha_{\text{app}}$  approaches  $\alpha_{\text{zircon-melt}}$  as  $f$  tends to 0; and iii) the magnitude of the offset between  $\alpha_{\text{true}}$  and  $\alpha_{\text{app}}$  is not significantly amplified (*i.e.*,  $\alpha_{\text{app}}$  become larger than  $\alpha_{\text{true}}$  by more than ~50%) for  $f$  values below 0.5. This means that  $\alpha_{\text{app}}$ , which can be easily calculated for each of our experiments, in all cases provides a maximum constraint on the magnitude of the true  $\alpha_{\text{zircon-melt}}$  governing the experiment.

#### Solution 2 – constraining $\alpha$ using $R_0$ and $R_{\text{liq}}$ , or $\alpha_{\text{liq}}$ :

By rearranging Eq. S-13 to solve for  $\alpha$ , one can obtain an expression that uses the measured compositions of the bulk system ( $R_0$ ) and the residual liquid ( $R_{\text{liq}}$ ) at a given  $f$  value to obtain a solution for  $\alpha_{\text{zircon-melt}}$ , which we call  $\alpha_{\text{liq}}$ .

$$\alpha_{\text{liq}} = \frac{\log\left(\frac{R_{\text{liq}}}{R_0}\right)}{\log(f)} + 1 \quad \text{Eq. S-18}$$

This analytical solution only considers the isotopic compositions of the bulk system ( $R_0$ ) and liquid ( $R_{\text{liq}}$ ), but ignores that of the cumulative zircon ( $R_{\text{bulk solid}}$ ).

#### Solution 3 – constraining $\alpha$ using $R_0$ and $R_{\text{bulk solid}}$ , or $\alpha_{\text{solid}}$ :

By rearranging Eq. S-15 and substituting Eq. S-13 to solve for  $\alpha$ , one obtains an expression that uses the measured compositions of the bulk system ( $R_0$ ) and the cumulative zircon ( $R_{\text{bulk solid}}$ ) at a given  $f$  value to solve for the effective  $\alpha_{\text{zircon-melt}}$ , which we call  $\alpha_{\text{solid}}$ .

$$\alpha_{\text{solid}} = \frac{\log\left(1 - \frac{(1-f)R_{\text{bulk solid}}}{R_0}\right)}{\log(f)} \quad \text{Eq. S-19}$$

In contrast to Solution 2, this analytical solution considers only the isotopic composition of the bulk system ( $R_0$ ) and the cumulative zircon ( $R_{\text{bulk solid}}$ ) but ignores that of the liquid ( $R_{\text{liq}}$ ).

#### Solution 4 – constraining $\alpha$ using $R_{\text{liq}}$ and $R_{\text{bulk solid}}$ , or $\alpha_{\text{glass-zircon}}$ :

Since Solution 2 ( $\alpha_{\text{liq}}$ ) and Solution 3 ( $\alpha_{\text{solid}}$ ) above do not consider both of the phases produced by each experiment, they consistently ignore important constraints on  $\alpha_{\text{zircon-melt}}$  imposed by our measured isotopic compositions. Therefore, we derive one last solution that uses both available constraints. In Solution 1 above,



we divided the composition of the measured cumulative solid ( $R_{\text{bulk solid}}$ ) by the liquid ( $R_{\text{liq}}$ ) to obtain  $\alpha_{\text{app}}$  (Eq. S-17). We can take this equation a step further by equating  $R_{\text{bulk solid}}$  and  $R_{\text{liq}}$  to their analytical solutions, Eqs. S-15 and S-13, respectively.

$$\frac{R_{\text{bulk solid}}}{R_{\text{liq}}} = \frac{R_0 - (R_0 f^{\alpha-1}) \cdot f}{(1-f)} \cdot \frac{1}{R_0 f^{\alpha-1}} \quad \text{Eq. S-20}$$

Solving for  $\alpha$ , one finds an expression that combines the measured compositions of the cumulative solid ( $R_{\text{bulk solid}}$ ), the liquid ( $R_{\text{liq}}$ ), and  $f$ , as follows:

$$\alpha_{\text{glass-zircon}} = \frac{\ln\left(\frac{1}{f + \frac{R_{\text{bulk solid}}(1-f)}{R_{\text{liq}}}}\right)}{\ln(f)} + 1 \quad \text{Eq. S-21}$$

Because this solution for  $\alpha$  considers most of the constraints our measurements impose on each experimental product, *i.e.*,  $R_{\text{bulk solid}}$ ,  $R_{\text{liq}}$ , and  $f$ , we favor the results obtained using this last solution whenever possible.

In this study, we test the four aforementioned approaches for constraining  $\alpha_{\text{zircon-melt}}$ , namely:  $\alpha_{\text{app}}$ ,  $\alpha_{\text{liq}}$ ,  $\alpha_{\text{solid}}$ , and  $\alpha_{\text{glass-zircon}}$ . In practice, we inverted Eqs. S-17, S-18, S-19 and S-20 using a Monte Carlo approach with  $10^4$  realizations, taking into consideration the uncertainties of all input parameters to output a mean  $\alpha$  for each method with a total propagated uncertainty. Uncertainties for each parameter were assumed to be normally distributed. For a system in perfect equilibrium, solutions 2, 3 and 4 should return equivalent values of  $\alpha$ . However, our modelling results summarized in Table S3 show that the samples are not in perfect equilibrium, as these different solutions do not always yield concordant  $\alpha$  values. Of all solutions,  $\alpha_{\text{liq}}$  and  $\alpha_{\text{solid}}$  consistently return modelled results that do not match the measured isotopic composition of the parameter left unconstrained by the calculations.  $\alpha_{\text{solid}}$  behaves as the worst solution, as it consistently violates the constraint that  $\alpha_{\text{app}}$  must be the maximum permissible  $\alpha$ . In contrast,  $\alpha_{\text{liq}}$  tends to underestimate the magnitude of fractionation because it does not consider the isotopic composition of the strongly fractionated solids. On the other hand, the solutions that we consider better reflect the isotopic results are  $\alpha_{\text{app}}$  or  $\alpha_{\text{glass-zircon}}$ . For samples with low  $f$  values ( $<0.5$ ), the  $\alpha_{\text{glass-zircon}}$  solution does not do an adequate job of capturing the unexpectedly low  $\delta^{94/90}\text{Zr}$  measured for the cumulative zircon which, as described in the main text and below, we argue has an isotopic composition dominated by kinetic isotope fractionation. Thus, for run products with  $f < 0.5$ ,  $\alpha_{\text{app}}$  was selected as the preferred solution, as it provides a *maximum* constraint on the magnitude of equilibrium isotope fractionation. We further note that, in the case of zircon crystallization, kinetic isotope fractionation during diffusion-limited growth implies that light Zr isotopes will be delivered more efficiently to a growing zircon seed than heavier isotopes, thereby making the cumulative solid lower in  $\delta^{94/90}\text{Zr}$  than expected from vibrational equilibrium alone (Watson and Müller, 2009; Meheut *et al.*, 2021) and amplifying the magnitude of  $\alpha_{\text{app}}$ . Thus, even though our low- $f$  experiments significantly depart from an equilibrium Rayleigh behavior due to kinetic isotope fractionation, both equilibrium and kinetic effects work in the same direction (*i.e.*, both make a zircon's  $\delta^{94/90}\text{Zr}$  'light'), and so  $\alpha_{\text{app}}$  from our experiments consistently provides a maximum permissible value for the magnitude of the  $\alpha_{\text{zircon-melt}}$  at equilibrium.

Figure S-4 shows the maximum constraints on the magnitude of isotopic fractionation for each experiment as imposed by Eq. S-17 ( $\alpha_{\text{app}}$ ), compared to the *ab initio* models of Chen *et al.* (2020) and Meheut *et al.* (2021).



In experiments with  $f < 0.5$ , kinetic isotope effects are dominant (see main text and next section for discussion), and so the magnitude of  $\alpha_{\text{app}}$  determined from these experimental products was preferred and considered as a maximum permissible value of  $\alpha_{\text{zircon-melt}}$ . For experiments with larger  $f$  values ( $> 0.5$ ), Solution 4, which takes into consideration all measured constraints for each experiment, was preferred. Accordingly, a preferred value for  $\alpha$  was selected for each experiment and this value is presented in Table S4. These values are the ones used for all figures and discussions throughout the main text.

### Numeric model for kinetic isotope fractionation during zircon growth

Bindeman and Melnik (2022) recently presented a numerical solution to the problem of kinetic Zr isotope fractionation during diffusion-limited zircon growth under variable conditions. To illustrate how kinetic isotope effects may affect the results of our experiments, we performed numerical calculations using a slightly adjusted version of the freely available code of Bindeman and Melnik (2022). The parameters used were as follows: 1) the velocity of the outermost boundary (*i.e.*, the ‘plagioclase front’ of Bindeman and Melnik (2022)) was set to zero, to account for the fact that no phases other than zircon were formed during our experiments and the outer capsule boundary remained in a static position; 2) the M-factor was set to 1.51, which is the middle of the range of our experiments and in agreement with base mixture GT02 used here (see Table S1); 3) because our higher T experiments were conducted at 1400 °C and this is the temperature at which experimental zircon nucleated (Wang and Trail, 2019), the bulk Zr concentration of the model was set to the concentration that would saturate zircon at this temperature given the prescribed M-factor and using the parameters of Boehnke *et al.* (2013), as used in the Bindeman and Melnik (2022) code. Because the zircon fractions analyzed here represent bulk cumulative zircon rather than instantaneous compositions, and the code of Bindeman and Melnik (2022) only outputs instantaneous solid compositions as a function of crystal radius, a simple addition was made to their code to compute the cumulative  $\delta^{94/90}\text{Zr}$  of zircon as a function of crystal radius by integrating the instantaneous zircon composition over a spherical geometry. The calculation performed here considered a temperature decrease of 50 K over the course of 120 hours, which was a typical experimental time for the runs of Wang and Trail (2019). Water contents were set to 10 wt. % as in the experiments of Wang and Trail (2019).

The results of the numerical simulation described above are shown graphically in Figure 2 in the main text and in Figure S-6. The curve in Figure 2 highlights the slope of the  $1000\ln(\alpha_{\text{zircon-melt}})$  vs.  $10^6/T$  relation that would result from a kinetic control on Zr isotope fractionation. In addition to the slope of this line reproducing well our results from the high-temperature (1300 – 1400 °C) experiments, this modeled line also crucially: i) *does not* intersect the origin of this graph as would be required by equilibrium isotope fractionation (*e.g.*, Young *et al.*, 2015); ii) *does not* resemble the slopes of the equilibrium fractionation models of Chen *et al.* (2020) and Méheut *et al.* (2021); and iii) has a slope that is much closer to the model proposed by Guo *et al.* (2020), which was derived by linearly fitting apparent  $\Delta^{94/90}\text{Zr}$  values obtained from Rayleigh inversion of  $\delta^{94/90}\text{Zr}$  zoning in natural zircon crystals. Altogether, these observations indicate that the low- $f$  experiments conducted at high temperature are strongly affected by non-equilibrium isotope fractionation. Figure S-6 shows other simulation outputs relevant to the run depicted in Figure 2 and/or that are useful scaling parameters to quantify the magnitude of non-equilibrium isotope fractionation (*e.g.*, Watson and Müller, 2009), namely (a) the calculated zircon radius vs. time, (b) zircon-melt Zr partition coefficient vs. time, (c) diffusivity (D) of Zr in the melt vs. time; d) calculated rate of zircon growth (*i.e.*, radial velocity of phase boundary migration, R) vs. crystal radius; e) R/D scaling parameter vs. crystal radius; and (f) resulting zircon  $\delta^{94/90}\text{Zr}$  vs. crystal radius relationship with curves for both instantaneous as well as cumulative zircon  $\delta^{94/90}\text{Zr}$  values.

## Supplementary Tables

**Table S-1** Experimental and compositional parameters of zircon growth experiments. Temperature (T), time (t), pressure (P).

Experiment	ZrGT51	ZrGT28	ZrGT26	ZrGT27	ZrGT33	ZrGT19	ZrGT17	ZrGT16	ZrGT13	ZrGT46	ZrGT01	ZrGT45	ZrGT02	ZrGT03
Base (Melt)	GT03	GT02	GT02	GT01	GT08	GT01	GT03	GT02	GT01	GT02	GT01	GT01	GT02	GT03
<i>T</i> (°C)	1300	1400	1300	1400	1400	1300	1150	1150	1150	1100	925	1100	925	925
<i>t</i> (hr)	120	120	120	120	120	120	312	312	312	288	120	288	120	120
<i>P</i> (GPa)	1.0	1.0	1.0	1.0	1.0	1.0	1.0	1.0	1.0	1.0	1.0	1.0	1.0	1.0
ASI melt	0.93	1.09	1.08	1.31	0.91	1.31	0.9	1.15	1.25	1.16	0.95	1.32	1.18	1.33
ASI melt, 1 s.d.	0.01	0.02	0.03	0.02	0.01	0.03	0.03	0.03	0.04	0.03	–	0.04	–	–
A/NK	1.42	1.7	1.64	2.04	1.37	2.04	1.41	1.84	1.95	1.76	1.52	2.02	1.97	2.24
A/NK, 1 s.d.	0.02	0.04	0.02	0.02	0.02	0.05	0.03	0.05	0.07	0.05	–	0.08	–	–
M	1.76	1.51	1.51	1.21	1.72	1.18	1.75	1.35	1.23	1.43	1.70	1.23	1.35	1.17
M 1, s.d.	0.03	0.03	0.05	0.02	0.02	0.02	0.07	0.03	0.04	0.06	–	0.04	–	–
Melt type	ML	PL	PL	PL	ML	PL	ML	PL	PL	PL	ML	PL	PL	PL
ZrO <sub>2</sub> (wt. %)	2.87	2.52	2.52	2.24	3.85	2.24	2.87	2.52	2.24	2.52	2.24	2.24	2.52	2.87
Zr (ppm)	21247	18656	18656	16583	28502	16583	21247	18656	16583	18656	16583	16583	18656	21247
<i>T</i> <sub>saturation</sub> (°C)	1560	1614	1614	1699	1680	1713	1563	1682	1690	1648	1501	1690	1681	1820
ln( <i>D</i> <sub>Zr</sub> )	3.15	3.28	3.28	3.40	2.86	3.40	3.15	3.28	3.40	3.28	3.40	3.40	3.28	3.15
<i>D</i> <sub>Zr</sub>	23.4	26.7	26.7	30.0	17.5	30.0	23.4	26.7	30.0	26.7	30.0	30.0	26.7	23.4



**Table S-2** Calculated values of Zr fractional removal ( $f$ ) from the liquid from mass-balance, ranked by increasing  $f$ 

Experiment Base (Melt)	ZrGT51 GT03	ZrGT28 GT02	ZrGT26 GT02	ZrGT27 GT01	ZrGT33 GT08	ZrGT19 GT01	ZrGT17 GT03	ZrGT16 GT02	ZrGT13 GT01	ZrGT46 GT02	ZrGT01 GT01	ZrGT45 GT01	ZrGT02 GT03	ZrGT03 GT02
Zr concentrations in glass measured by SIMS and resulting $f$ values (means and standard deviations)														
[Zr] <sub>glass</sub> (μg/g)	18760	16074	15528	13621	21290	7827	5088	3050	2370	1873	1699	1534	794	601
s.d.	592	869	362	727	494	2710	551	196	151	89	60	48	35	58
$f_{Zr-glass}$	0.12	0.14	0.17	0.18	0.25	0.53	0.76	0.84	0.86	0.90	0.90	0.91	0.963	0.97
s.d.	0.06	0.09	0.04	0.09	0.03	0.33	0.05	0.02	0.02	0.01	0.01	0.01	0.003	0.01
Zr/Rb concentration ratios in bulk-glass aliquots produced from acid leaching, and resulting mean $f$ calculations														
(Zr/Rb) <sub>bulk</sub>	42.49	37.31	37.31	33.17	57.00	33.17	42.49	37.31	33.17	37.31	33.17	33.17	42.49	37.31
(Zr/Rb) <sub>glass</sub>	35.40	31.03	30.01	26.05	42.45	15.15	8.61	4.71	3.85	3.58	2.73	2.66	1.39	2.57
[Rb] <sub>bulk</sub> (μg/g)	500	500	500	500	500	500	500	500	500	500	500	500	500	500
[Zr] <sub>bulk</sub> (μg/g)	21247	18656	18656	16583	28502	16583	21247	18656	16583	18656	16583	16583	21247	18656
[Zr] <sub>zircon</sub> (μg/g)	497661	497661	497661	497661	497661	497661	497661	497661	497661	497661	497661	497661	497661	497661
$X_{glass}$	0.9929	0.9937	0.9927	0.9929	0.9854	0.9819	0.9660	0.9672	0.9705	0.9661	0.9694	0.9693	0.9587	0.9651
$X_{zircon}$	0.0071	0.0063	0.0073	0.0071	0.0146	0.0181	0.0340	0.0328	0.0295	0.0339	0.0306	0.0307	0.0413	0.0349
$f_{Zr/Rb}$	0.17	0.17	0.20	0.21	0.26	0.54	0.80	0.87	0.88	0.90	0.92	0.92	0.97	0.93
	<b>High-T, Low-<math>f</math></b>						<b>Low-T, High-<math>f</math></b>							



**Table S-3** Zr isotope results for all base mix, glass, and zircon fractions analyzed.

Experiment	ZrGT51	ZrGT28	ZrGT26	ZrGT27	ZrGT33	ZrGT19	ZrGT17	ZrGT16	ZrGT13	ZrGT46	ZrGT01	ZrGT45	ZrGT02	ZrGT03
<b>Base mix</b> ( $\delta^{94/90}\text{Zr}$ )	-0.057	-0.052	-0.052	-0.054	-0.059	-0.054	-0.057	-0.052	-0.054	-0.052	-0.054	-0.054	-0.052	-0.057
2SE	0.007	0.005	0.005	0.007	0.010	0.007	0.007	0.005	0.007	0.005	0.007	0.007	0.005	0.007
n	14	27	27	14	8	14	14	27	14	27	14	14	27	14
MSWD	0.67	1.06	1.06	0.90	0.78	0.90	0.67	1.06	0.90	1.06	0.90	0.90	1.06	0.67
<b>Glass</b> ( $\delta^{94/90}\text{Zr}$ )	-0.055	-0.052	-0.057	-0.051	-0.050	-0.054	0.123	0.052	0.044	0.091	-0.004	0.060	0.062	0.054
2SE	0.013	0.016	0.016	0.013	0.013	0.013	0.013	0.013	0.011	0.013	0.013	0.013	0.013	0.013
n	5	4	4	6	6	5	5	5	6	5	5	5	6	5
MSWD	1.36	0.95	0.53	0.59	0.43	0.88	1.48	1.07	1.68	0.38	0.82	1.01	1.60	0.34
<b>Zircon</b> ( $\delta^{94/90}\text{Zr}$ )	-0.158	-0.116	-0.168	-0.135	-0.068	-0.128	-0.138	-0.115	-0.115	-0.084	-0.094	-0.084	-0.074	-0.088
2SE	0.011	0.009	0.011	0.011	0.013	0.011	0.013	0.013	0.011	0.013	0.011	0.011	0.011	0.013
n	7	9	6	6	6	6	5	5	6	5	6	6	6	5
MSWD	1.48	0.27	0.55	0.29	0.56	0.83	1.64	0.62	1.29	0.28	1.50	0.74	0.06	0.49





**Table S-4** Calculated values of  $f$  and  $\Delta^{94/90}\text{Zr}$  from Monte Carlo inversion of Zr isotope results, ranked by increasing  $f$ . Solutions 1 through 4, as described in the supplementary text, are expressed as  $1000 \times \ln(\alpha)$ . **Values in red** have calculated  $1000 \times \ln(\alpha)$  magnitudes larger than  $1000 \times \ln(\alpha_{\text{app}})$ , and thus violate the constraint that  $1000 \times \ln(\alpha_{\text{app}})$  provides a maximum permissible value for the  $1000 \times \ln(\alpha_{\text{zircon-melt}})$  of each experiment.

Experiment	ZrGT51	ZrGT28	ZrGT26	ZrGT27	ZrGT33	ZrGT19	ZrGT17	ZrGT16	ZrGT13	ZrGT46	ZrGT01	ZrGT45	ZrGT02	ZrGT03
Mass fraction of Zr removed from liquid														
$f_{\text{Zr-glass}}$	0.12	0.14	0.17	0.18	0.25	0.53	0.76	0.84	0.86	0.90	0.90	0.91	0.96	0.97
$\pm$ s.d.	0.06	0.09	0.04	0.09	0.03	0.33	0.05	0.02	0.02	0.01	0.01	0.01	0.00	0.01
<b>Solution 1</b> – $\alpha_{\text{app}}$ from Eq. S-17														
$\Delta^{94/90}\text{Zr}_{\text{zircon-melt}}$	-0.103	-0.064	-0.111	-0.084	-0.018	-0.074	-0.261	-0.167	-0.159	-0.175	-0.090	-0.144	-0.136	-0.142
$\pm$ 2s	0.017	0.018	0.019	0.017	0.018	0.017	0.018	0.018	0.016	0.018	0.019	0.017	0.017	0.020
<b>Solution 2</b> – $\alpha_{\text{liq}}$ from Eq. S-18														
$\Delta^{94/90}\text{Zr}_{\text{zircon-melt}}$	-0.016	-0.013	0.016	-0.015	-0.031	0.000	-0.126	-0.057	-0.050	-0.062	-0.022	-0.048	-0.035	-0.032
$\pm$ 2s	1.463	18.841	3.027	7.467	0.088	0.630	0.083	0.018	0.015	0.012	0.007	0.008	0.006	0.009
<b>Solution 3</b> – $\alpha_{\text{solid}}$ from Eq. S-19														
$\Delta^{94/90}\text{Zr}_{\text{zircon-melt}}$	-0.108	-0.067	-0.125	-0.090	-0.010	-0.110	-0.180	-0.178	-0.188	-0.125	-0.154	-0.124	-0.172	-0.271
$\pm$ 2s	0.022	0.020	0.017	0.027	0.019	0.813	2.773	0.079	0.093	0.068	0.066	0.059	0.109	0.433
<b>Solution 4</b> – $\alpha_{\text{glass-zircon}}$ from Eq. S-21														
$\Delta^{94/90}\text{Zr}_{\text{zircon-melt}}$	-0.097	-0.059	-0.101	-0.076	-0.016	-0.052	-0.139	-0.077	-0.070	-0.068	-0.035	-0.055	-0.040	-0.040
$\pm$ 2s	0.020	0.021	0.019	0.022	0.016	0.062	0.054	0.016	0.014	0.011	0.008	0.008	0.006	0.010
	<b>High-T, Low-<math>f</math></b>						<b>Low-T, High-<math>f</math></b>							



**Table S-5** Summary of preferred  $f$ ,  $\alpha$ , and  $\Delta^{94/90}\text{Zr}$  values from all experiments used for figures in the main text.

Experiment	ZrGT51	ZrGT28	ZrGT26	ZrGT27	ZrGT33	ZrGT19	ZrGT17	ZrGT16	ZrGT13	ZrGT46	ZrGT01	ZrGT45	ZrGT02	ZrGT03
<i>mean f</i>	0.12	0.14	0.17	0.18	0.25	0.53	0.76	0.84	0.86	0.90	0.90	0.91	0.96	0.97
Solution method	app	app	app	app	app	app	glass-zircon	glass-zircon	glass-zircon	glass-zircon	glass-zircon	glass-zircon	glass-zircon	glass-zircon
$\alpha$	0.999897	0.999936	0.999889	0.999916	0.999982	0.999926	0.999861	0.999923	0.999930	0.999932	0.999965	0.999945	0.999960	0.999960
2s	0.000017	0.000018	0.000019	0.000017	0.000018	0.000017	0.000054	0.000016	0.000014	0.000011	0.000008	0.000008	0.000006	0.000010
$\Delta^{94/90}\text{Zr}_{\text{zircon-melt}}$	-0.103	-0.064	-0.111	-0.084	-0.018	-0.074	-0.139	-0.077	-0.070	-0.068	-0.035	-0.055	-0.040	-0.040
2s	0.017	0.018	0.019	0.017	0.018	0.017	0.054	0.016	0.014	0.011	0.008	0.008	0.006	0.010
	<b>High-T, Low-f</b>						<b>Low-T, High-f</b>							



## Supplementary Figures

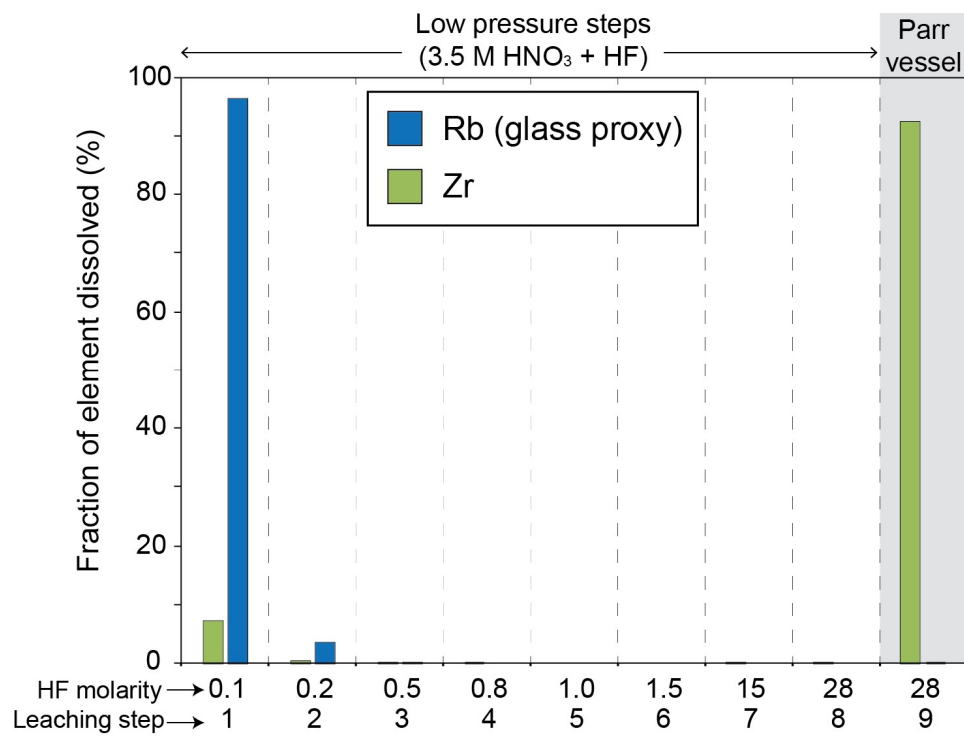


**Figure S-1** Calibrated separation procedure using the fraction of total Rb and Zr measured in the supernatant from each step as a proxy for zircon-glass separation. Complete glass dissolution is achieved using 0.1 and 0.2 M HF steps at low pressure, while zircon is not reacted until using 28 M HF in a Parr® vessel.

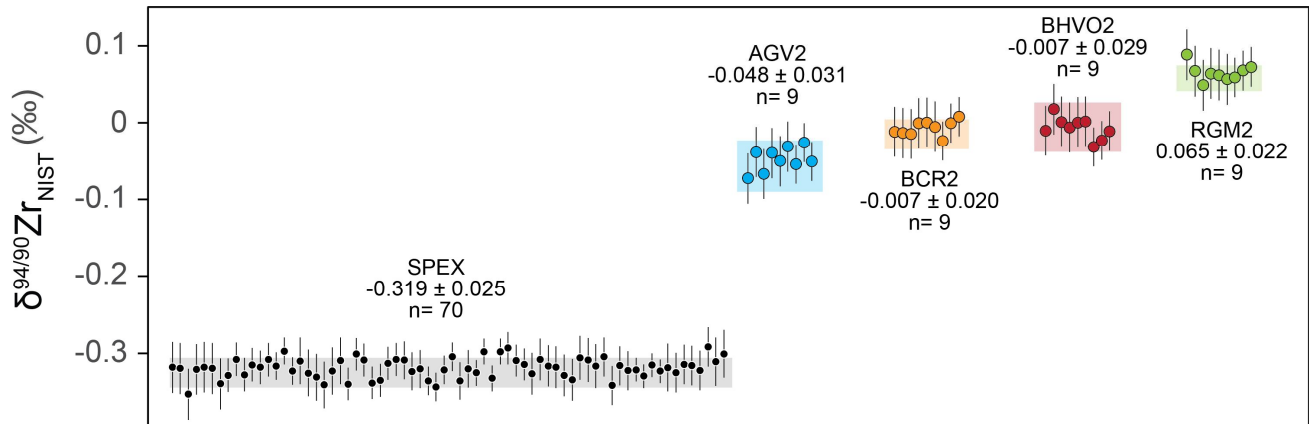


**Figure S-2** Results of Zr reference materials measured during this study, reported as  $\delta^{94/90}\text{Zr}_{\text{NIST}}$ . The reported values are unweighted means and uncertainties are 2 standard deviations of the data. Shaded bars represent the reference values for each material considering results published in the literature and our long-term reproducibility, as follows: SPEX:  $-0.325 \pm 0.019$  ‰; AGV2:  $-0.057 \pm 0.034$  ‰; BCR2:  $-0.015 \pm 0.019$  ‰; BHVO2:  $-0.006 \pm 0.032$  ‰; RGM2:  $0.058 \pm 0.016$  ‰.

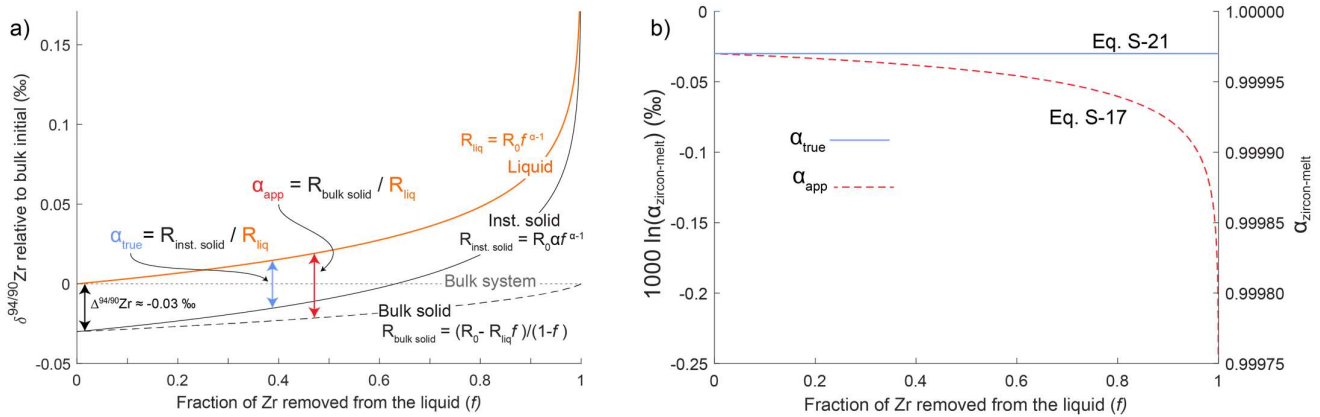


**Figure S-3 a)** Forward model showing the isotopic evolution of a Rayleigh system as a function of Zr removal from the liquid ( $f$ ) where  $1000 \ln \alpha_{\text{zircon-melt}} \approx 0.03$ , or  $\alpha = 0.99997$ . The dotted grey line represents the initial bulk system, the solid black line represents the instantaneous solid, the dashed black line represents the bulk solid, and the orange line represents the liquid. Also shown are equations S-13 through S-17. **b)** Calculated values of  $\alpha_{\text{zircon-melt}}$  (solid blue line), the true isotopic fractionation coefficient of the system according to Eq. S-4, and  $\alpha_{\text{app}}$  (red dashed line), the apparent isotopic fractionation coefficient calculated from our experiments according to Eq. S-5, from the forward model of panel a.  $\alpha_{\text{app}}$  approaches  $\alpha_{\text{zircon-melt}}$  as  $f$  tends to 0 and increases with increasing  $f$ , meaning that  $\alpha_{\text{app}}$  always provides a maximum constraint on the magnitude of  $\alpha_{\text{zircon-melt}}$ . Note that the divergence between  $\alpha_{\text{zircon-melt}}$  and  $\alpha_{\text{app}}$  increases drastically after  $f > 0.5$



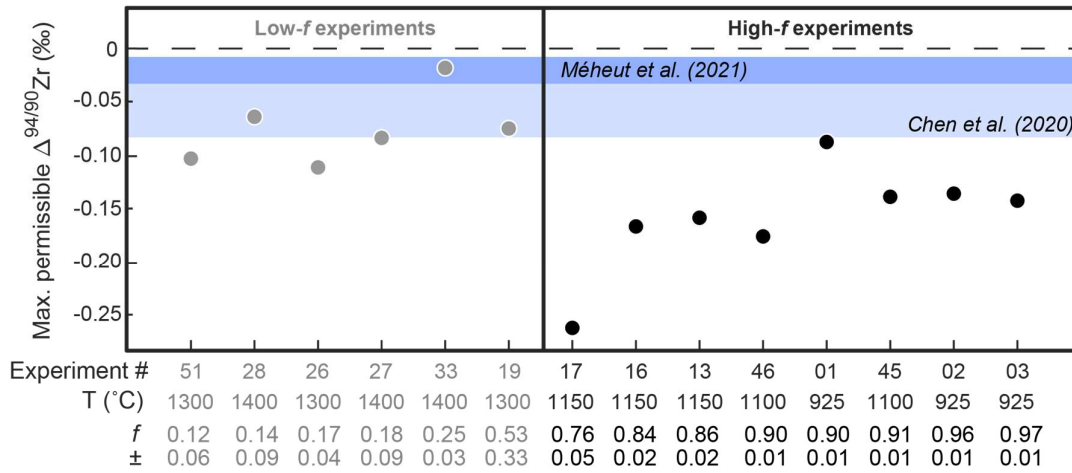


**Figure S-4** Magnitude of  $\alpha_{app}$ , the maximum permissible value for the effective  $\alpha_{zircon-melt}$  governing each experiment, as a function of  $f$  for all our experimental products. Note that larger magnitudes of  $\alpha_{app}$  for high- $f$  experiments are expected, given the strong dependence of  $\alpha_{app}$  with  $f$  for Rayleigh systems with  $f > 0.5$  (Fig. S3b).

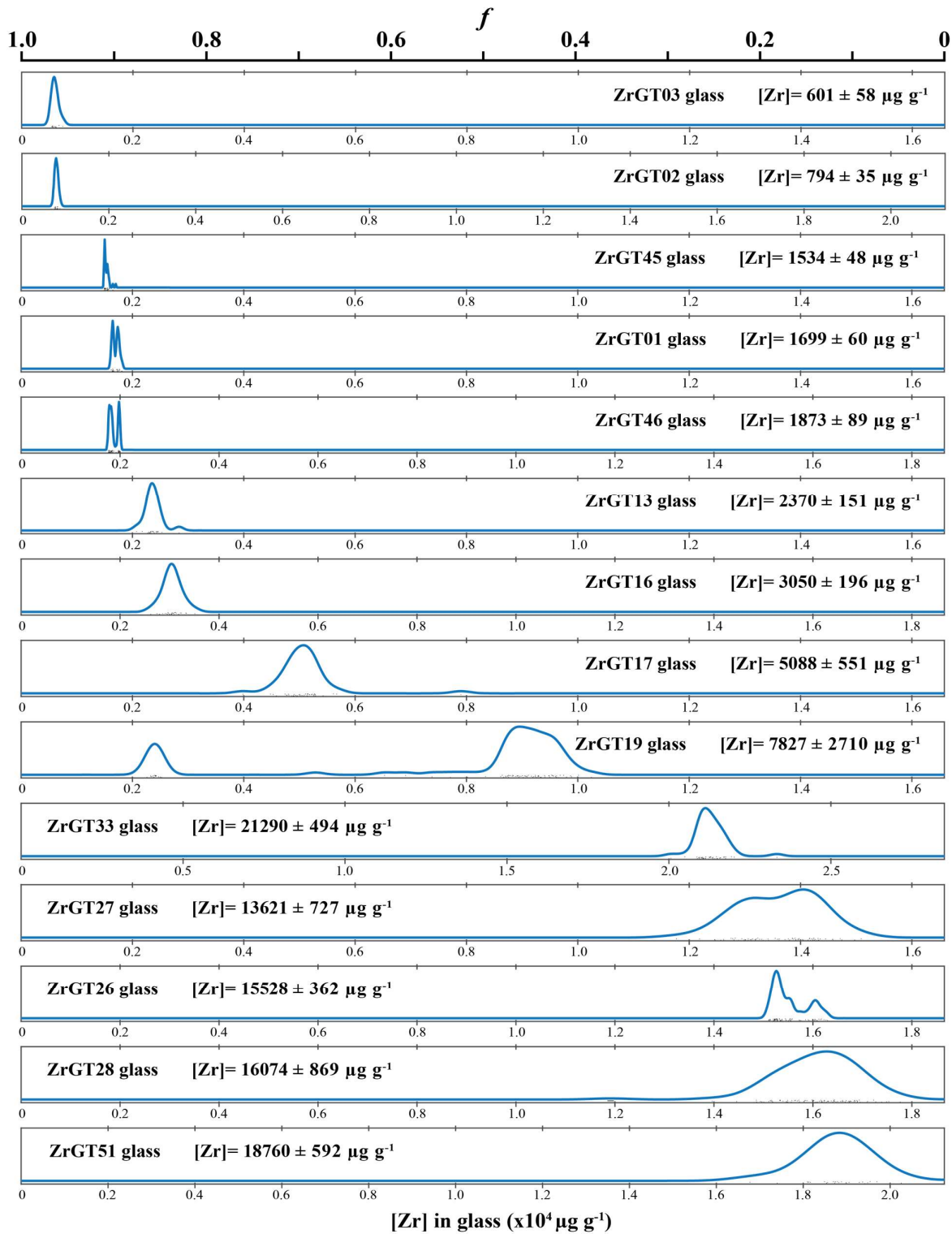


**Figure S-5** Kernel probability density estimates showing the spatial variability of Zr concentration values (bottom axis) and  $f$  values (top axis) within the glass in each experiment, calculated using  $n=20-90$  single-spot SIMS measurements in glass fragments.

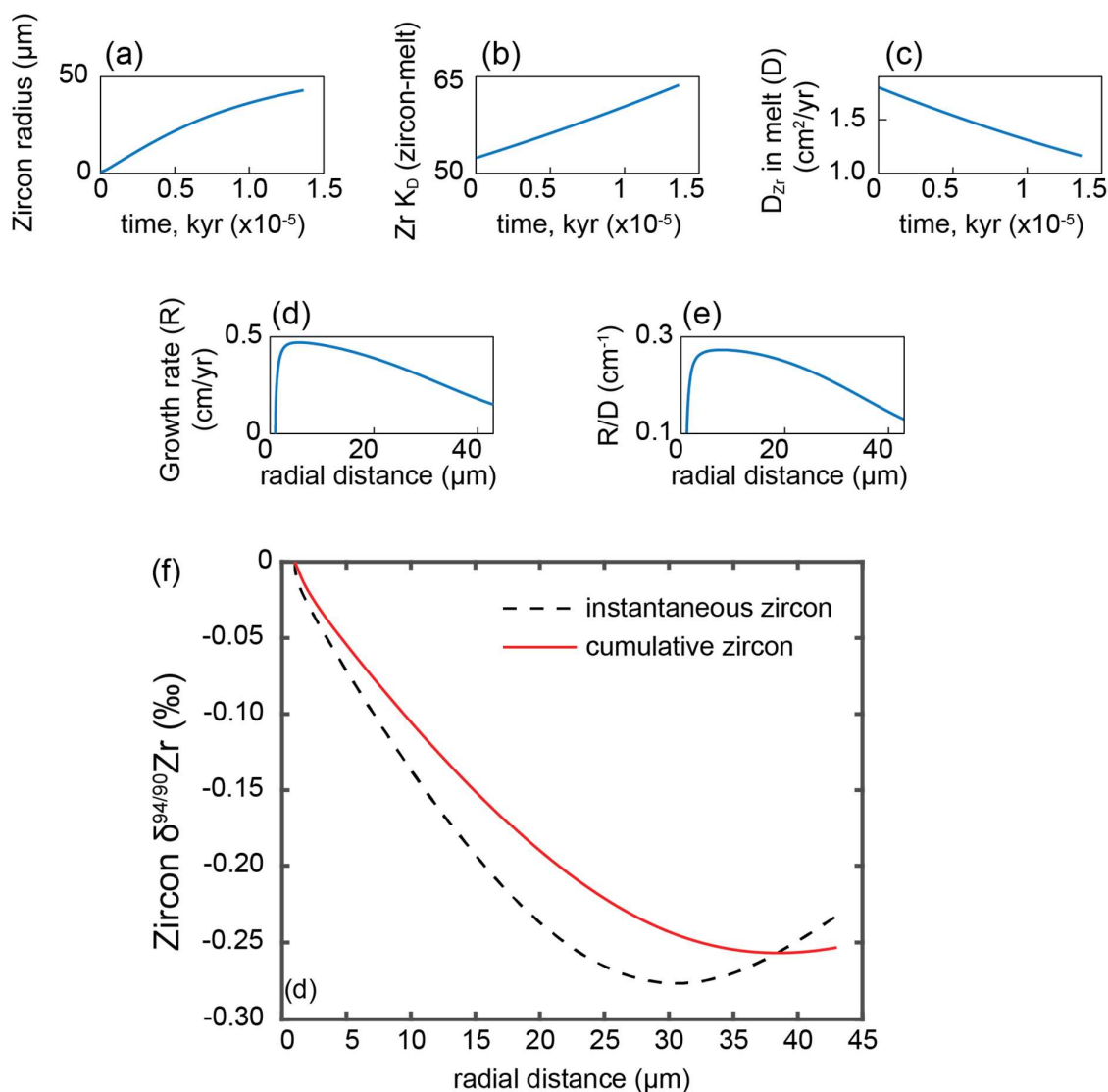


**Figure S-6** Results of kinetic Zr isotope fractionation numerical model, performed using the code of Bindeman and Melnik (2022) using parameters described in the supplementary text. Outputs shown are: a) zircon radius (μm) vs. time (kyr x 10<sup>-5</sup>); b) Zircon-melt Zr partition coefficient (K<sub>D</sub>) vs. time (kyr x 10<sup>-5</sup>); c) Zr diffusivity in the melt (D; cm<sup>2</sup>/yr) vs. time (kyr x 10<sup>-5</sup>); d) zircon growth rate (R; cm/yr) vs. crystal radial distance (μm); e) radial velocity of grain boundary migration over Zr diffusivity in the melt (R/D; cm<sup>-1</sup>) vs. crystal radial distance (μm); and f) cumulative (solid red line) and instantaneous (dashed black line) zircon δ<sup>94/90</sup>Zr values vs. crystal radial distance. Results shown in Figure 3 are depicted as the 1000ln(α) vs. 10<sup>6</sup>/T (K) relation of this model output for the cumulative zircon composition.

## Supplementary Information References

- Bindeman, I.N. and Melnik, O.E. (2022) The rises and falls of zirconium isotopes during zircon crystallisation. *Geochemical Perspectives Letters* 24, 17–21. <https://doi.org/10.7185/geochemlet.2241>
- Botev, Z.I., Grotowski, J.F. and Kroese, D.P. (2010) Kernel density estimation via diffusion. *The Annals of Statistics* 38, 2916–2957. <https://doi.org/10.1214/10-AOS799>
- Boehnke, P., Watson, E.B., Trail, D., Harrison, T.M. and Schmitt, A.K. (2013) Zircon saturation re-visited. *Chemical Geology* 351, 324–334. <https://doi.org/10.1016/j.chemgeo.2013.05.028>
- Chen, X., Wang, W., Zhang, Z., Nie, N.X. and Dauphas, N. (2020) Evidence from Ab Initio and Transport Modeling for Diffusion-Driven Zirconium Isotopic Fractionation in Igneous Rocks. *ACS Earth and Space Chemistry* 4, 1572–1595. <https://doi.org/10.1021/acsearthspacechem.0c00146>
- Criss, R.E. (1999) Principles of Stable Isotope Distribution. Oxford Univ Press, New York. <https://doi.org/10.1093/oso/9780195117752.001.0001>
- Guo, J.L., Wang, Z., Zhang, W., Ducea, M.N. (2020) Significant Zr isotope variations in single zircon grains recording magma evolution history. *Proceedings of the National Academy of Sciences* 117, 21125–21131. <https://doi.org/10.1073/pnas.2002053117>
- Klaver, M., Ibañez-Mejía, M., Tissot, F. L. H., Vroon, P. Z. and Millet, M.-A. (2021) Reliability of detrital marine sediments as proxy for continental crust composition: The effects of hydrodynamic sorting on Ti and Zr isotope systematics. *Geochimica et Cosmochimica Acta* 310, 221–239. <https://doi.org/10.1016/j.gca.2021.05.030>
- Méheut, M., Ibañez-Mejía, M., and Tissot, F.L.H. (2021) Drivers of zirconium isotope fractionation in Zr-bearing phases and melts: The roles of vibrational, nuclear field shift and diffusive effects. *Geochimica et Cosmochimica Acta* 292, 217–234. <https://doi.org/10.1016/j.gca.2020.09.028>
- Pourmand, A., and Dauphas, N. (2010) Distribution coefficients of 60 elements on TODGA resin: Application to Ca, Lu, Hf, U and Th isotope geochemistry. *Talanta* 81, 741–753. <https://doi.org/10.1016/j.talanta.2010.01.008>
- Pullen, A., Ibañez-Mejía, M., Gehrels, G.E., Ibañez-Mejía, J.C. and Pecha, M. (2014) What happens when n= 1000? Creating large-n geochronological datasets with LA-ICP-MS for geologic investigations. *Journal of Analytical Atomic Spectrometry* 29, 971. <https://doi.org/10.1039/C4JA00024B>
- Thomas, J.B., Bodnar, R.J., Shimizu, N., and Sinha, A. K. (2002) Determination of zircon/melt trace element partition coefficients from SIMS analysis of melt inclusions in zircon. *Geochimica et Cosmochimica Acta*, 66, 2887–2901. [https://doi.org/10.1016/S0016-7037\(02\)00881-5](https://doi.org/10.1016/S0016-7037(02)00881-5)
- Tissot, F.L.H., Ibañez-Mejía, M., Vocke, R., Rabb, S., Fehr, M., Schönbacher, M., Tang, H., Young, E. (2022) Establishing and calibrating the Zr isotope Reference Material (iRM). Goldschmidt abstract 9653, Hawaii, US. <https://doi.org/10.46427/gold2022.9653>
- Tompkins, H.G.D., Zieman, L.J., Ibañez-Mejía, M., and Tissot, F.L.H. (2020) Zirconium stable isotope analysis of zircon by MC-ICP-MS: Methods and application to evaluating intra-crystalline zonation in a zircon megacryst. *Journal of Analytical Atomic Spectrometry* 35, 1167–1186. <https://doi.org/10.1039/C9JA00315K>
- Wang, Y., and Trail, D. (2019) Aluminum partitioning between zircon and haplogranitic melts: The influence of temperature and melt composition. *Chemical Geology* 511, 71–80. <https://doi.org/10.1016/j.chemgeo.2019.02.016>
- Watkins, J.M., DePaolo, D.J. and Watson, E.B. (2017) Kinetic Fractionation of Non-Traditional Stable Isotopes by Diffusion and Crystal Growth Reactions. *Reviews in Mineralogy and Geochemistry* 82, 85–125. <https://doi.org/10.2138/rmg.2017.82.4>
- Watson, E.B. and Müller, T. (2009) Non-equilibrium isotopic and elemental fractionation during diffusion-controlled crystal growth under static and dynamic conditions. *Chemical Geology* 267, 111–124. <https://doi.org/10.1016/j.chemgeo.2008.10.036>

Young, E.D. Manning, C.E., Schauble, E.A., Shahar, A., Macris, C.A., Lazar, C., and Jordan, M. (2015) High-temperature equilibrium isotope fractionation of non-traditional stable isotopes: Experiments, theory, and applications. *Chemical Geology* 395, 176–195.  
<https://doi.org/10.1016/j.chemgeo.2014.12.013>

